Quantifying the 3D macrostructure of tissue scaffolds

**Julian R. Jones · Robert C. Atwood ·
Gowsihan Poologasundarampillai · Sheng Yue ·
Peter D. Lee**

Abstract The need to shift from tissue replacement to
tissue regeneration has led to the development of tissue
engineering and in situ tissue regeneration. Both of these
strategies often employ the use of scaffolds—templates
that allow cells to attach and then guide the new tissue
growth. There are many design criteria for an ideal scaf-
fold. These criteria vary depending on the tissue type and
location in the body. In any application of a scaffold it is
vital to be able to characterise the scaffold before it goes
into in vitro testing. In vitro testing allows the cell
response to be investigated before its in vivo performance
is assessed. A full characterisation of events in vitro and
in vivo, in three dimensions (3D), is necessary if a scaf-
fold's performance and effectiveness is to be fully
quantified. This paper focuses on porous scaffolds for bone
regeneration, suggests appropriate design criteria for a
bone regenerating scaffold and then reviews techniques for
obtaining the vitally important quantification of its pore
structure. The techniques discussed will include newly
developed methods of quantifying X-ray microtomography
(μCT) images in 3D and for predicting the scaffolds
mechanical properties and the likely paths of fluid flow
(and hence potential cell migration). The complications in
investigating scaffold performance in vitro are then dis-
cussed. Finally, the use of μCT for imaging scaffolds for
in vivo tests is reviewed.

1 Introduction

The aim of regenerative medicine is to restore diseased or
damaged tissue to its original state and function. There are
two main strategies to achieve this aim; tissue engineering
and in situ tissue regeneration. Both of these strategies
frequently use scaffolds to guide and stimulate cells to
generate new tissue [1, 2]. An ideal method of tissue
engineering bone is harvesting osteogenic cells from the
patient, which are then expanded in culture and seeded on a
scaffold that acts as both a guide and stimulus for tissue
growth in three dimensions [3, 4]. The second strategy,
in situ tissue regeneration, is implemented by implanting a
resorbable scaffold directly into a defect site and the body is
employed as its own bioreactor [1, 3]. In each case, the
synthetic scaffold should resorb into the body as non-toxic
degradation products, allowing the bone to remodel itself
into mature bone structure. Whichever strategy is used, if an
optimal scaffold is to be designed, criteria to base the design
on, and methods of quantifying how well these criteria are
met, are required. This is the focus of this paper. The exact
cell type that should be used for bone tissue engineering is
also a matter of contention and a subject for further inves-
tigation. The length of time the cells should be cultured
before implantation will depend on the cell type used, but is
also a matter of much discussion. In any event, to be able to
determine the best cell source, cellular response studies on
promising scaffolds must be carried out, and that response
characterised. This is non-trivial and will be discussed later.

2 An ideal scaffold for bone regeneration?

There are many criteria for an ideal scaffold for bone tissue
engineering [1, 5]. One of the most important is that a

J. R. Jones (✉) · R. C. Atwood · G. Poologasundarampillai ·
S. Yue · P. D. Lee
Department of Materials, Imperial College London,
London SW7 2BP, UK
e-mail: julian.r.jones@imperial.ac.uk

biocompatible scaffold has a highly interconnected porous network with both pore sizes, and interconnections, large enough for cell migration, fluid exchange and eventually tissue ingrowth and vascularisation (penetration of blood vessels). In order for bone to grow into a scaffold, the interconnected pore network is thought to need pores and interconnects with diameters in excess of 100 μm [6]. Methods for quantifying the pore network are the subject of this review.

The scaffold should also: bond to the host bone without the formation of a fibrous capsule; deliver factors that stimulate the body's own regenerative mechanisms to produce new bone; and resorb safely into the body at the same rate as the bone regenerates, leaving little trace of a defect [7]. The new bone will need to remodel under loading as the scaffold resorbs. Many defect sites are subjected to load, and load is necessary if the bone is to remodel successfully, therefore an ideal scaffold should also be able to withstand the loading environment until the regenerated tissue can take the load, without being so stiff it shields surrounding bone from this load.

In summary, a scaffold is required that matches the morphology and properties of bone as closely as possible. Achieving all these properties in one material is a complex challenge. To make it possible the scaffold materials must be optimised from the atomic level through the nanoscale to the macroscale with respect to cellular response. This paper will begin by describing how the interconnected pore network of scaffolds can be characterised, including determining the mechanical properties and permeability non-destructively.

3 Quantification of interconnected porous networks

It is vital to be able to fully quantify the pore network of scaffolds in 3D. The pore network will affect permeability, which will affect how body fluid penetrates, the rate of cell migration and vascularised bone ingrowth. The most common parameter that is quoted to describe the pore network of scaffolds is "porosity" or more accurately percentage porosity, which is calculated using the following [8]:

$$\%P = 1 - (\rho_b / \rho_s) \qquad (1)$$

where ρ_b is the bulk density and ρ_s is the skeletal density. ρ_b can be measured geometrically, ρ_s can measured using helium pycnometry. Percentage porosity is used because it is relatively easy to obtain. However, for a tissue scaffold, percentage porosity is often meaningless. Arguably the most important parameter are the diameter and shape of the interconnects between pores.

A traditional method of imaging pores is to use scanning electron microscopy (SEM). SEM micrographs can be misleading as they are images of fracture surfaces; therefore the real 3D shape and connectivity of the pores cannot be imaged or quantified without using stereology. Unless a field emission gun (FEG) SEM is available, polymeric and ceramic scaffolds have to be coated, making the technique destructive. Historically, the pore size distributions of materials have been measured by mercury intrusion porosimetry (MIP), which applies the Washburn equation to changes in capacitance as it is forced into the scaffolds as a function of pressure [9]. Although pore size distributions are obtained, these distributions confound the effects of both pore and interconnect size. The model applied to the porogram data (the raw data which is volume of mercury intruded as a function of pressure) provides information on the constrictions on mercury flow into the material, i.e. it provides only an indirect indication of the interconnect distribution in a pore network and no information on shape. MIP is also destructive as the samples are contaminated with mercury. It is, however still an essential tool that must be used as a benchmark and validation tool for new techniques.

A recently developed technique which can be non-destructive uses X-ray microtomography (μCT), which can produce 3D images of porous scaffolds. It works by collecting a series of two dimensional (2D) transmission X-ray images as a sample rotates within an X-ray beam. These images are converted via a process known as filtered backprojection to form a three dimensional (3D) reconstructed image [10]. In laboratory source μCT systems geometric enlargement is used to magnify the image by placing the object close to a micron sized spot source, producing a magnified image which is projected onto a solid-state detector a large distance from the object (relative to the source-object distance). In synchrotron μCT systems a parallel beam is normally used and magnification is obtained via the optics coupling the X-ray detecting phosphor and CCD camera. Both systems provide quantitative data on the integrated density and atomic number of the matter in each voxel (volume pixel). Figure 1 shows μCT images of human trabecular bone (a) and a bioactive glass scaffold (b).

Bioactive glass is a good candidate material for regenerative scaffolds because it bonds to bone, dissolves in the body and releases Si and Ca ions that stimulate bone cells at the genetic level [7, 11]. Bone bonding is achieved by the formation of a nanoscale hydroxycarbonate apatite (HCA) layer on the glass surface on contact with body fluid [12]. HCA is very similar to the apatite in bone and therefore forms a bond. The bioactive glass scaffold in Fig. 1b was produced by foaming sol–gel derived bioactive glasses using the process described previously [5, 13, 14]. Figure 1 shows, qualitatively, that the 3D pore structure of the scaffold is similar to that of trabecular bone. Using

Fig. 1 X-ray microtomography images of (**a**) human trabecular bone and (**b**) a bioactive glass scaffold
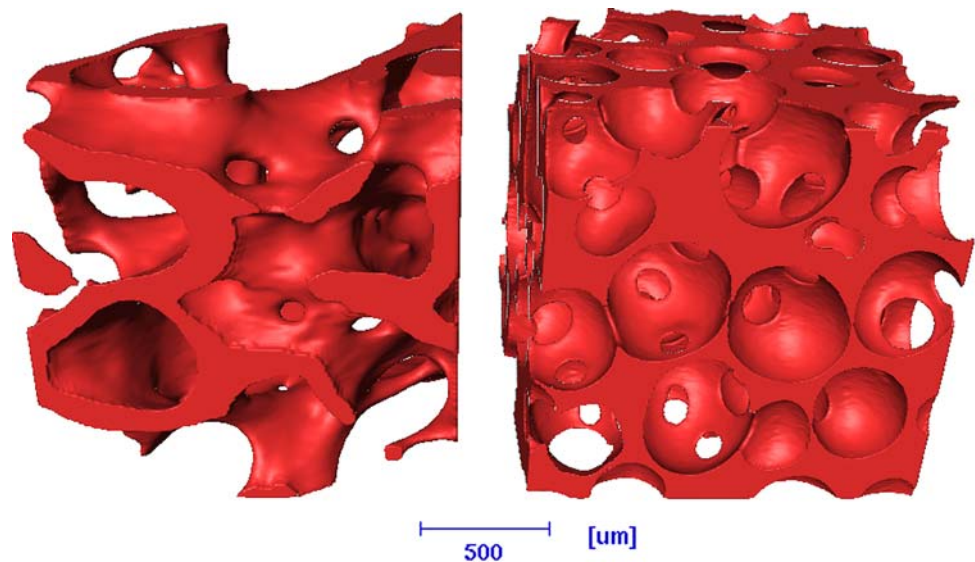
visualization software, it is possible to move a cutting plane through the scaffold to gain a qualitative understanding of the shape of the pores, how they are interconnected and the tortuosity of the path from the outer edge of the sample to the centre. Many research facilities now have μCT and many research groups in the field of tissue engineering show 3D images, but to scientifically access a scaffold, quantitative descriptors are required rather than qualitative comparisons. The most important criteria for the pore network of a tissue scaffold is interconnection size and number. Only through the use of μCT is it currently possible to quantify the difference between different potential scaffolds, or even to provide quality assurance between successive manufacturing batches of the same scaffold materials. Therefore, μCT screening of implants before clinical trials allows a greater level of quality assurance than many other techniques.

4 Quantitative 3D analysis of μCT images

The parameters that are desirable from a μCT image of a scaffold are pore size, pore interconnect diameter and some measure of interconnectivity. Interconnectivity can be defined as the number of connections (over a certain diameter) per pore. Another parameter of interest is the tortuosity, which could be quantified as the number of interconnects a cell would have to pass through to reach the centre of the scaffold. This can of course vary depending on the path taken. There are very few complete quantitative measures of the interconnected pore networks in scaffolds with connected pores, but there have been several studies on methods of quantifying percentage porosity [15] and pore size [16–19]. Work was also done on quantifying

mineral formation within polymer scaffolds, e.g. apatite formation within a collagen gel in a bioreactor as a function of time, using the difference in attenuation (density) between the mineral formed and the scaffold [20]. However, none of these papers addressed methods for obtaining the size or shape of the interconnects.

Moore et al. [21] did quantify some parameters of the pore network by analysing μCT images of a polymer scaffold produced by the salt-leaching process. They calculated the volume fraction of porosity that was connected from one face of the scaffold to another via a minimum interconnect size. However, they did not determine the size distribution of either the pores or interconnects present. Otsuki et al. [22] calculated the path length from the surface to connected interior pores using a well established algorithm developed for percolation studies in rock [23]. Combining this with a dilation algorithm, they grouped pore throats based on the rate of closure of the paths of connection. However, they did not quantify individual pores and interconnects.

The quantification of individual pores and interconnects has been achieved by the current authors, who developed a new approach, built on a combination of established algorithms, to produce an in-house code that allows each individual pore and interconnect throughout the entire network to be characterised in 3D, creating size and morphology distributions for all the pores and interconnects within a scaffold [14, 24]. This novel algorithm is based on first calculating the distance each point (termed a voxel in 3D, like a pixel in a 2D image) within a pore is from its nearest strut. Next these values are used as a "distance map" upon which a algorithm can be applied to separate out individual pores from each other via the gradient in the distance map, termed a watershed algorithm as it is

analogous to water flowing downhill (effectively towards the struts).

Before the distance map could be calculated, the grey-scale µCT datasets were thresholded to determine which voxels were scaffold material and which were air. Successive dilation operations were then applied to calculate the distance travelled in from the edge of the pore (in equal steps) until all air voxels are filled. Voxels with the greatest local value are the point of greatest distance from the wall and hence are the centre of each local pore. This operation produces a distance map from the edge of the pores to the centroids of the pores. A 3D watershed algorithm [25] was then applied to the distance map to divide the interconnected porous space by finding the valleys in the distance maps, allowing identification of individual pores. The watershed algorithm included a low pass filter to remove the tiny valleys created by noise. The interconnects between pores are then easily identified as contiguous groupings of voxels with neighbours on the same two pores. Finally, the individual pores and interconnects were quantified to determine their volume (pores) or area (interconnects) and maximum diameter.

The application of this algorithm to a bioactive glass foam is illustrated in Fig. 2, showing 2D cross-sections from the µCT dataset where each pore was identified and coloured separately. Although both scaffolds in Fig. 2a, b had the same percentage porosity (85%) and were prepared in similar ways, µCT combined with analysis illustrates that their pore networks are clearly different. Figure 2a shows a scaffold with large connected pores ideal for a tissue scaffold. The network was quite homogeneous. The sample in Fig. 2b was poured too close to the gelling point and it has a heterogeneous pore network with one large pore and many smaller pores. The pore network would be too closed for cell migration and tissue growth. This heterogeneous distribution was caused by pouring the foam into the mould too close to its gelling point. Figure 3 shows the pore size and interconnect size distributions (effective radius) of the foams obtained using the dilation and watershed algorithms. Figure 3 shows that the heterogeneous foam has some large pores but few smaller pores (Fig. 3a) and that the homogeneous foam had many larger pores. Figure 3b shows that the interconnects in the heterogeneous foam were generally smaller than those in the homogeneous foam, showing that the heterogeneous foam is not suitable for bone tissue engineering applications.

The technique was demonstrated on a bioactive glass foam scaffold to track changes as a function of processing, together with calculations of the flow properties, providing the data required for future bioreactor design. It has also been demonstrated to work on other materials, for example titanium foams [26].
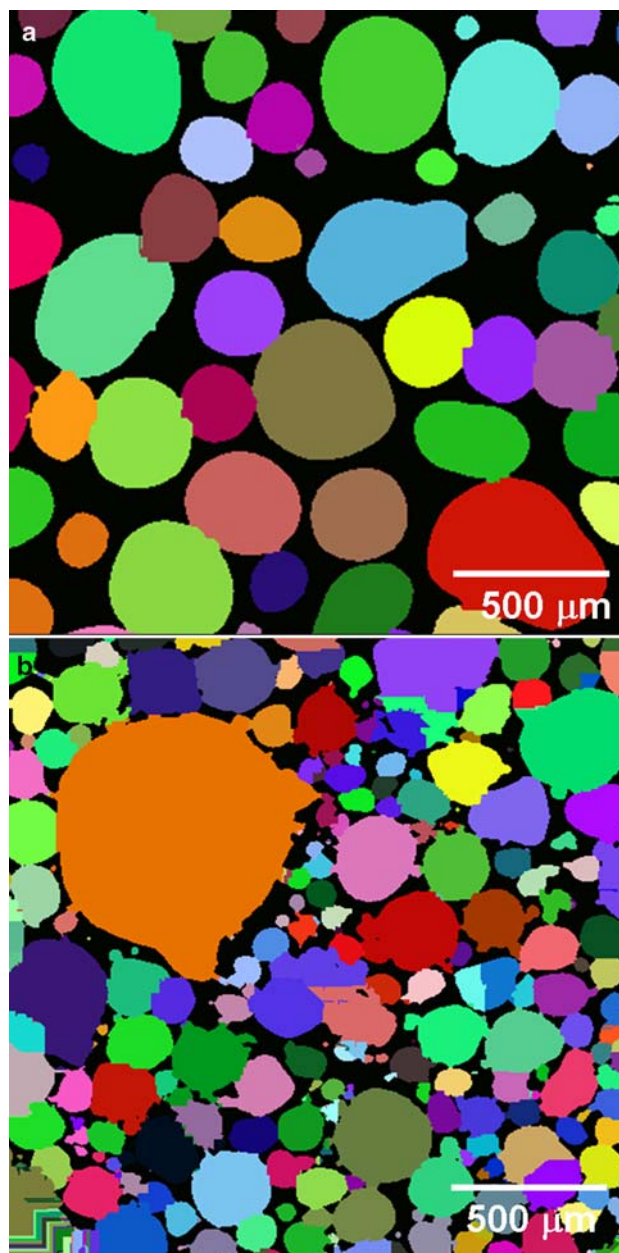

Fig. 2 X-ray microtomography (µCT) images (2D slices) of two bioactive glass scaffolds (**a**) with a homogeneous pore structure and (**b**) with a bimodal pore network

5 Mechanical properties

The pore structure and geometry of a material will affect its mechanical properties, for example a porous ceramic will have a stiffness (Young's modulus) much lower than a solid block of the same material.

Images obtained by µCT can therefore be used to predict the mechanical properties of materials and effects of pore architecture in individual scaffolds, if the corresponding properties of the bulk material are known. Measuring the mechanical properties of the scaffolds as a function of the
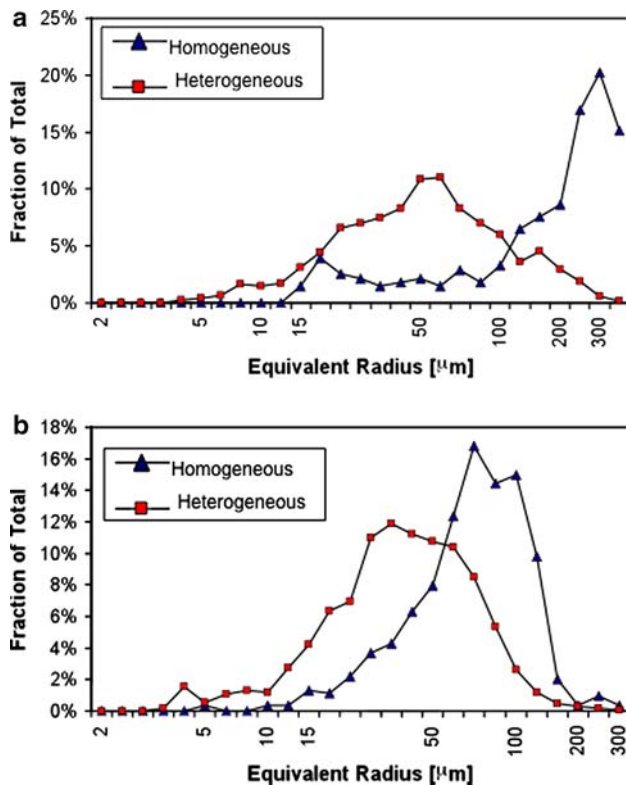
Fig. 3 (**a**) Pore, and (**b**) interconnect radius distributions of bioactive glass scaffolds, calculated using image analysis techniques on μCT images

scaffold pore structure and degradation is a difficult, time consuming and destructive process. Stiffness is normally measured by compression testing in the elastic regime requiring specimens with smooth parallel faces evenly distributing the load. However, with foam structures it is very difficult to cut parallel faces, and even if this is achieved, the inherently irregular structure of the struts means local plasticity occurs very quickly. Although non-destructive measurements would be ideal, the application of ultrasonic measurement of stiffness in foams is still highly specialised and has yet to be applied to many foamed materials. An alternative is predictive modelling based on the pore architecture. The μCT data can be meshed and input into finite element models. In addition to stiffness, the stresses and strains at the scaffold–cell interface, which can be related to bone formation observed in the μCT images, have been calculated [27–29]. The advantage of this process over conventional testing is that it is non-destructive and it takes into account the pore architecture of individual materials.

6 Permeability and fluid flow

For degradable scaffolds, the rate of flow through the material will affect the degradation rate. Perhaps more importantly, differences in flow rate within a scaffold can cause differential degradation rates. For bioactive glass and ceramic scaffolds, areas with higher flow rates are likely to degrade more rapidly than areas of low flow. This may be the opposite for polyester scaffolds. Fluid will always flow along the route of least resistance. During in vitro cell culture, the flow of culture medium containing cells during cell seeding is critical to developing an evenly populated scaffold. In vivo, it is vital that there are paths for cells to migrate, tissue to grow in and waster products to flow.

The flow in a porous material at a macroscopic level can be described by the generalised tensor form of Darcy's law, allowing the bulk velocity to be related to the change in pressure using what is called the permeability tensor, $\overline{K}$. Therefore, $\overline{K}$ provides a quantitative descriptor of the ease at which fluid (culture medium or blood) will penetrate the scaffold. Using the 3D geometry of the scaffold's pore network obtained via μCT, a microscale flow simulation can be run. The flow within porous medium obeys Stokes equations at the local scale so the permeability can be calculated using the geometry and by numerically solving Stokes equations [14]. Streaklines can be plotted and superimposed onto the μCT image of the pore network or perhaps more usefully on a 3D image of the interconnects with the scaffold and macropore network removed (Fig. 4). This technique allows non-destructive observations of areas of dominant flow within an individual scaffold. The flow path and rate is dominated by the size of the interconnects and their orientation relative to the direction of the flow.

7 In vitro cellular response

Conventional cell biology studies of cellular response to growth factors or drugs involve the culture of cells in well plates, often on thin tissue culture plastic slides, which are optically transparent. This is termed 2D culture. This allows the use of inverted optical microscopes to be used to visualize cell behaviour. However, when cells are grown on a 3D material, optical microscopes are ineffective in imaging the cells. Cell function in 3D is very different to 2D so it is vital to be able to determine how introducing macropores to material affects the cell response [30]. SEM can be used to observe cell morphology on fracture surfaces, as can immunohistochemistry techniques using fluorescence confocal microscopy, however the depth of field of confocal microscopy is limited to ∼100 μm. Bioceramic scaffolds also have the added problem of autofluorescence. The easiest method for analyzing cell response on 3D scaffolds is to lyse (remove) the cells and analyse the lysates for protein expression [31]. Improved techniques are therefore needed to be able to image cellular response within 3D matrices.

Fig. 4 Predicted Stokes flow (from top to bottom face) through a bioactive glass scaffold with only the flow and interconnects visualized. Scale bar in microns

μCT can be used to monitor the mineralisation of osteiod within a scaffold. The first study to show this was by Cartmell et al. [17], who measured the amount and location of bone tissue formation in polymer scaffolds over time. The scaffolds were seeded with rat stromal cells or calvarial cells, cultured for 8 weeks, and scanned at weekly intervals. Increased bone formation was observed over time with no effects of radiation during μCT scanning.

Using time lapsed μCT imaging, Hagenmüller et al. investigated the formation of bone mineral from human mesenchymal stem cells (hMSC) cultured on silk fibrin scaffolds in osteogenic medium over 44 days [32]. Parameters such as the bone volume density (bone volume fraction within the scaffold), trabecular thickness and spacing were assessed. Tissue mineral density was determined only within the segmented bone volume.

8 In vivo

For in vivo tests or clinical trials it is imperative to know the exact structure of the pore network before and after implantation, therefore a non-destructive

characterisation technique is required for quantification. After explantation, information on how the scaffold pore network has changed and the amount and quality of tissue that has grown into the scaffold is needed. This can include the number of blood vessels, whether the vessels are intact or leaky and amount of bone growth and degree of mineralisation within the scaffold. As μCT imaging is non-destructive, explanted samples are available for histology after scanning. However, quantification of the images is needed. This is non-trivial. There is difficulty in accurately separating the multiple phases within a scaffold.

8.1 Bone tissue ingrowth

Immediately after implantation, a scaffold will contain clotting blood. After a time, osteogenic cells will lay down organic matrix. The matrix will then mineralise. Therefore, as time passes, varying levels of mineralized tissue exist within the scaffold. This complex process makes it difficult to identify different phases within tomographic images based on density information alone, especially if the scaffold is a similar material to the ingrowing bone. The most common method is based on choice of attenuation thresholds [33]; however, this can lead to misidentification of voxels, especially to those of the tissue, which will have an attenuation between that of a ceramic scaffold and air. For example, it is difficult to isolate small volumes of bone formed on the surface of bioceramic scaffolds. The density of newly formed bone matrix is lower than that of mature bone. Quantification of bone ingrowth can therefore be highly sensitive to the chosen threshold value. A simple way to avoid this is to maintain a consistent selected threshold value within an experiment, but this is not always possible if the scaffold is degrading and losing density over time, as this will affect the image's relative greyscale intensity.

A more advanced segmentation method is therefore needed. Hilldore et al. [34] used osmium tetroxide staining, to enhance the attenuation of unmineralised osteoid on hydroxyapatite scaffolds, with curve integration of the attenuation. However, the use of stains is not always appropriate. Jones et al. [35] employed a three-phase segmentation approach to obtain images showing separation of bone tissue within hydroxyapatite scaffolds following implantation into sheep tibia. Their segmentation procedure used a multistep filter with anisotropic diffusion and edge enhancement followed by a converging active contours algorithm. The segmentation algorithm particularly utilised information within the intensity-gradient histogram. The attenuation distributions resulting from the segmentation approach for pore, bone, and scaffold overlap.

Porosity, pore size distributions, interconnect sizes and distribution of bone ingrowth in the explanted scaffolds were then measured. Pore size was measured using a maximal covering spheres (MCS) algorithm, with the pore size defined as the radius of the largest sphere that enclosed within the pore space. They then overlaid the bone ingrowth phase and measured the bone voxels within the pores. To quantify bone ingrowth as a function of accessible pore size they used the invasion or capillary radius. It gives the smallest pore constriction between the scaffold edge and any voxel within the scaffold pore space. The capillary radius was measured by applying a capillary drainage simulation on the 3D tomographic image. They observed that bone ingrowth occurs primarily at the periphery of the scaffold. The accessible pore size was strongly correlated to bone ingrowth, with a strong enhancement of bone ingrowth for pore diameters >100 μm. For new bone to survive, it must contain a vasculature. Imaging and quantifying vessels and bone is an even greater challenge.

Many groups are using dual X-ray energy scans (sometimes termed dual-energy X-ray absorptiometry or DXA) to characterise the mineralisation of bone and teeth, a technique which takes advantage of elements having different attenuations at different X-ray energies and has been applied to hydroxyapatite [36] and, more recently, silk scaffolds in bone defects [37, 38].

8.2 Vasculature within scaffolds

Due to their low attenuation and small diameter, blood vessels are difficult to image in μCT. Radio-opaque contrast agents have enabled the visualization of microvasculature in tissues [39, 40], including the large vascular architecture in an entire mouse brain [41, 42], vasculature within bone fracture healing [43] and segmental cortical bone graft transplantations [44]. However none of these studies involved quantification of the vasculature or the imaging of newly formed vessels in tissue engineering constructs.

Duvall et al. [45] used contrast-enhanced μCT analysis to quantify morphologic parameters, including vessel volume, thickness, number, connectivity, and degree of anisotropy of a 3D vascular network. Briefly, the technique involves perfusion of a radiodense silicone rubber contrast agent containing lead chromate and a curing agent (Microfil MV-122, Flow Tech, Carver, MA) through the vasculature immediately following euthanasia. The explanted samples were demineralised prior to scanning, to allow segmentation of the vascular structures.

Bolland et al. [46] also used the "Microfil" technique to study angiogenesis in an impaction bone graft model. The grafts were produced by culturing human bone marrow stromal cells (HBMSC) on natural allograft bone and on synthetic poly lactide scaffolds. The constructs were implanted subcutaneously in immunosuppressed mice for 28 days. Microfil was perfused through the anaesthetised mice by injecting it into the heart. The mice were then placed in a refrigerator at 4°C for 2 h to trigger the polymerisation. Explanted and fixed samples were then scanned using a laboratory μCT scanner. Analysis of 3D reconstructions demonstrated an order of magnitude increase in vessel volume and vessel number in the scaffolds seeded with HBMC compared to scaffolds implanted without cells. The results were validated by immunohistochemistry and histology. Segmentation tools within the VG Studio Max 1.2.1 software package (Volume Graphics, GmbH, and Heidelberg, Germany) were used. Quantification of several parameters within the scaffolds was achieved: total vessel volume; volume of vessels/volume of scaffold; vessel thickness; mean number of vessels per unit length; and spacing between the vessels. The density (attenuation) of Microfil was used to obtain the total vessel volume (total number of voxels corresponding to Microfil) within each sample. Algorithms developed for bone structural material parameters by VG Studio Max were applied to the greyscale values corresponding to the microfil material. Vessel thickness (VTh) was determined by the ratio of vessel surface (VS) to the vessel volume (VV) and was calculated using the Cauchy–Crofton theorem i.e. $VTh = 2/BS/BV$, where BS is the bone surface and BV is the bone volume. The mean number of vessels per unit length (VN) was calculated using $VN = (BV/TV)/VTh$, where TV is the total number of vessels. The vessel spacing (VSp) between vessel structures which depends was determined using $VSp = 1/VN - VTh$.

9 Problems

Micro-computed tomography has many advantages, but like any technique, it also has many limitations and difficulties. A key limitation is that shared by any imaging technique, the field of view (fov) and resolution are intimately linked by the number of pixels in the detector. If a resolution of 1 μm is required and the detector is 1000 pixels in width, the maximum fov is 1 mm. Further, the highest quality reconstructions are only obtained when the entire object is in this fov, limiting the specimen size to 1 mm in diameter. This limitation can be overcome by either moving the detector or using region of interest reconstruction techniques; however both of these either significantly increase the acquisition time or reduce the image quality.

Another limitation of most tomographic systems is that only variations in X-ray attenuation can be detected, rather

than interfaces. Further, if there are a range of materials with widely varying attenuations, resolving the low attenuating material may be difficult. This makes the imaging of polymer scaffolds in mixed bone and soft-tissue structures difficult, as the attenuation of the polymer is close to the soft tissue when compared to bone. One method for overcoming this is the use of phase contrast tomography [47], which takes advantage of the fact that the refractive index changes rapidly at interfaces. This enables boundaries between similar attenuating materials to be distinguished, and is especially effective in soft-solids such as tissue and polymer scaffold systems. Unfortunately this technique is primarily used with coherent monochromatic sources, i.e. at synchrotrons.

Laboratory μCT systems usually have nominal resolutions in the range of 2–100 μm, where the resolution is dependent upon trade-offs between X-ray flux, field of view, and detector size/type. Specimens diameters can therefore range from 1 to over 100 mm, linked to the resolution required as explained above. For higher resolution, a synchrotron must be used to supply the X-rays. Synchrotron μCT has been used to image bone growth into injectable calcium phosphate scaffolds that were implanted in rabbit femurs [48]. Not only did the 3D reconstructions distinguish between new bone ingrowth, the material and connective tissue, but the high resolution (down to 0.1 μm) even allowed identification of osteocyte lacunae in the bone. However, there is a trade off as the field of view in synchrotron is small, meaning this technique is limited to relatively small samples (<1 mm^3).

The lack of validating studies in challenging pre-clinical models has made it difficult to determine which of the many available strategies to use clinically. Histology continues to be the standard method for the evaluation of biomaterial/tissue interfaces.

10 Summary

Recent advances in lab based μCT development has allowed high resolution (micron range) 3D imaging of scaffolds designed for regenerative medicine. Now, there is a shift of emphasis from improving the imaging techniques, to developing new and improved image analysis techniques to get the most from the 3D images. Quantification of the images is now possible, but more development of these computational techniques are needed to allow quantification of unusual pore networks, of 3D cell response in vitro and bone and blood vessel ingrowth, including quality of the blood vessels.

References

1. R. Langer, J.P. Vacanti, Science **260**, 920–926 (1993). doi:10.1126/science.8493529
2. E. Lavik, R. Langer, Appl. Microbiol. Biotechnol. **65**, 1–8 (2004). doi:10.1007/s00253-004-1580-z
3. H. Ohgushi, A.I. Caplan, J. Biomed. Mater. Res. **48**, 913–927 (1999). doi:10.1002/(SICI)1097-4636(1999)48:6<913::AID-JBM22>3.0.CO;2-0
4. T. Takezawa, Biomaterials **24**, 2267–2275 (2003). doi:10.1016/S0142-9612(03)00038-3
5. J.R. Jones, L.M. Ehrenfried, L.L. Hench, Biomaterials **27**, 964–973 (2006). doi:10.1016/j.biomaterials.2005.07.017
6. S.F. Hulbert, S.J. Morrison, J.J. Klawitte, J. Biomed. Mater. Res. **6**, 347–374 (1972). doi:10.1002/jbm.820060505
7. L.L. Hench, J.M. Polak, Science **295**, 1014–1017 (2002). doi:10.1126/science.1067404
8. L.J. Gibson, M.F. Ashby, *Cellular Solids Structure and Properties* (Pergamon Press, Oxford, 1988)
9. S. Lowell, J.E. Shields, Powder Technol. **38**, 121–124 (1984). doi:10.1016/0032-5910(84)80041-8
10. A.C. Kak, M. Slaney, *Principles of Computerized Tomographic Imaging* (IEEE Press, London, 1987)
11. I.D. Xynos, A.J. Edgar, L.D.K. Buttery, L.L. Hench, J.M. Polak, J. Biomed. Mater. Res. **55**, 151–157 (2001). doi:10.1002/1097-4636(200105)55:2<151::AID-JBM1001>3.0.CO;2-D
12. L.L. Hench, R.J. Splinter, W.C. Allen, T.K. Greenlee, J. Biomed. Mater. Res. **5**, 117–141 (1971). doi:10.1002/jbm.820050611
13. P. Sepulveda, J.R. Jones, L.L. Hench, J. Biomed. Mater. Res. **59**, 340–348 (2002). doi:10.1002/jbm.1250
14. J.R. Jones, G. Poologasundarampillai, R.C. Atwood, D. Bernard, P.D. Lee, Biomaterials **28**(7), 1404–1413 (2007)
15. Y. Hiu-Yan, Q. Ling, L. Kwong-Man, Z. Ming, L. Kwok-Sui, C.J. Chun-yiu, J. Biomed. Mater. Res. B Appl. Biomater. **75**, 234–242 (2005). doi:10.1002/jbm.b.30240
16. A.S.P. Lin, T.H. Barrows, S.H. Cartmell, R.E. Guldberg, Biomaterials **24**, 481–489 (2003). doi:10.1016/S0142-9612(02)00361-7
17. S. Cartmell, K. Huynh, A. Lin, S. Nagaraja, R. Guldberg, J. Biomed. Mater. Res. A **69A**, 97–104 (2004). doi:10.1002/jbm.a.20118
18. S.T. Ho, D.W. Hutmacher, Biomaterials **27**, 1362–1376 (2006). doi:10.1016/j.biomaterials.2005.08.035
19. R. Al-Raoush, K.A. Alshibli, Physica A **361**, 441–456 (2006). doi:10.1016/j.physa.2005.05.043
20. B.D. Porter, A.S.P. Lin, A. Peister, D. Hutmacher, R.E. Guldberg, Biomaterials **28**, 2525–2533 (2007). doi:10.1016/j.biomaterials.2007.01.013
21. M.J. Moore, E. Jabbari, E.L. Ritman, L.C. Lu, B.L. Currier, A.J. Windebank et al., J. Biomed. Mater. Res. A **71A**, 258–267 (2004). doi:10.1002/jbm.a.30138
22. B. Otsuki, M. Takemoto, S. Fujibayashi, M. Neo, T. Kokubo, T. Nakamura, Biomaterials **27**, 5871–5966 (2006). doi:10.1016/j.biomaterials.2006.08.013
23. D. Stauffer, *Percolation Theory* (Taylor and Francis, London, 1985)
24. R.C. Atwood, J.R. Jones, P.D. Lee, L.L. Hench, Scr. Mater. **51**, 1029–1033 (2004). doi:10.1016/j.scriptamat.2004.08.014
25. A.P. Mangan, R.T. Whitaker, IEEE Trans. Vis. Comput. Graph. **5**, 308–321 (1999). doi:10.1109/2945.817348
26. R. Singh, P.D. Lee, T.C. Lindley, R.J. Dashwood, E. Ferrie, T. Imwinkelried, Acta Biomater. (2008). doi:10.1016/j.actbio.2008.06.014

27. S.V.N. Jaecques, H. Van Oosterwyck, L. Muraru, T. Van Cley-nenbreugel, E. De Smet, M. Wevers et al., Biomaterials **25**, 1683–1696 (2004). doi:10.1016/S0142-9612(03)00516-7

28. D. Lacroix, A. Chateau, M.P. Ginebra, J.A. Planell, Biomaterials **27**, 5326–5334 (2006). doi:10.1016/j.biomaterials.2006.06.009

29. J.R. Jones, P.D. Lee, L.L. Hench, Philos. Trans. R. Soc. Lond. A **364**, 263–281 (2006). doi:10.1098/rsta.2005.1689

30. J.R. Jones, Mater. Today **9**, 34–43 (2006). doi:10.1016/S1369-7021(06)71741-2

31. J.R. Jones, O. Tsigkou, E.E. Coates, M.M. Stevens, J.M. Polak, L.L. Hench, Biomaterials **28**, 1653–1663 (2007). doi:10.1016/j.biomaterials.2006.11.022

32. H. Hagenmueller, S. Hofmann, T. Kohler, H.P. Merkle, D.L. Kaplan, G. Vunjak-Novakovic et al., Ann. Biomed. Eng. **35**, 1657–1667 (2007). doi:10.1007/s10439-007-9338-2

33. T. Hara, E. Tanck, J. Homminga, R. Huiskes, Bone **31**, 107–109 (2002). doi:10.1016/S8756-3282(02)00782-2

34. A. Hilldore, A. Wojtowicz, A.W. Johnson, J. Biomed. Mater. Res. A **82A**, 1012–1021 (2007). doi:10.1002/jbm.a.31264

35. A.C. Jones, C.H. Arns, A.P. Sheppard, D.W. Hutmacher, B.K. Milthorpe, M.A. Knackstedt, Biomaterials **28**, 2491–2504 (2007). doi:10.1016/j.biomaterials.2007.01.046

36. S. Grampp, D. Felsemberg, G. Furhmann, U. Gross, K.J. Wolff, E.F.G. Ring (eds.), *Current Research in Ostaeoporosis and Bone Mineral Measurement II* (British Institute of Radiology, London, 1992)

37. R. Mosheiff, B.Y. Klein, I. Leichter, G. Chaimsky, A. Nyska, A. Peyser et al., Biomaterials **13**, 462–466 (1992). doi:10.1016/0142-9612(92)90167-M

38. C. Kirker-Head, V. Karageorgiou, S. Hofmann, R. Fajardo, O. Betz, H.P. Merkle, M. Hilbe, B. von Rechenberg, J. McCool, L. Abrahamsen, A. Nazarian, E. Cory, M. Curtis, D. Kaplan, L. Meinel, Bone **41**, 247–255 (2007)

39. E. Toyota, K. Fujimoto, Y. Ogasawara, T. Kajita, F. Shigeto, T. Matsumoto, M. Goto, F. Kajiya, Circulation **105**, 621–626 (2002)

40. F. Plouraboue, P. Cloetens, C. Fonta, A. Steyer, F. Lauwers, J.P. Marc-Vergnes, J. Microsc.-Oxf. **215**, 139–148 (2004)

41. S. Heinzer, T. Krucker, M. Stampanoni, R. Abela, E.P. Meyer, A. Schuler, P. Schneider, R. Muller, Neuroimage **32**, 626–636 (2006)

42. S. Heinzer, G. Kuhn, T. Krucker, E. Meyer, A. Ulmann-Schuler, M. Stampanoni, M. Gassmann, H.H. Marti, R. Muller, J. Vogel, Neuroimage **39**, 1549–1558 (2008)

43. T. Miclau, C. Lu, Z. Thompson, P. Choi, C. Puttlitz, R. Marcucio, J.A. Helms, J. Orthop. Res. **25**, 1552–1558 (2007)

44. X.P. Zhang, C. Xie, A.S.P. Lin, H. Ito, H. Awad, J.R. Lieberman, P.T. Rubery, E.M. Schwarz, R.J. O'Keefe, R.E. Guldberg, J. Bone. Miner. Res. **20**, 2124–2137 (2005)

45. C.L. Duvall, W.R. Taylor, D. Weiss, R.E. Guldberg, Am. J. Physiol. Heart Circ. Physiol. **287**, H302–H310 (2004)

46. B.J.R.F. Bolland, J.M. Kanczler, D.G. Dunlop, R.O.C. Oreffo, Bone **43**, 195–202 (2008)

47. P. Tafforeau, R. Boistel, E. Boller, A. Bravin, M. Brunet, Y. Chaimanee, P. Cloetens, M. Feist, J. Hoszowska, J.J. Jaeger, R.F. Kay, V. Lazzari, L. Marivaux, A. Nel, C. Nemoz, X. Thibault, P. Vignaud, S. Zabler, Appl. Phys. A **83**, 195–202 (2006)

48. P. Weiss, L. Obadia, D. Magne, X. Bourges, C. Rau, T. Weitkamp, I. Khairoun, J.M. Bouler, D. Chappard, O. Gauthier, G. Daculsi, Biomaterials **24**, 4591–4601 (2003)